Computational/Experimental Study of the Flowfield on a Body of Revolution at Incidence

G. G. Zilliac*
NASA Ames Research Center, Moffett Field, California

A joint computational-experimental study of the vortical flowfield on a pointed body of revolution is undertaken. The incompressible Navier-Stokes equations are solved numerically for steady flow around an ogive-cylinder at angle of attack. The three-dimensional vortical flow is investigated, with emphasis on the tip and the near-wake region. Comparisons of computational results with results of a companion towing-tank experiment are presented at $Re_L = 1000$. Results of a wind tunnel experiment at $Re_L = 820{,}000$ featuring use of a seven-hole pressure probe also are presented. It was observed that at the low Reynolds number of the towing tank study, the leeside flow was symmetric at the angles of attack considered. For the same configuration at the higher Reynolds number of the wind tunnel study, the flow was asymmetric under equivalent conditions for some of the angles of attack studied. The topology of the flow is discussed and conclusions are drawn concerning the growth and stability of the primary vortices.

Nomenclature

C_f	= skin-friction coefficient
C_p	= pressure coefficient
D	= maximum diameter of body
L	= length of body
r	= direction normal to surface
Re_D	= Reynolds number based on D
Re_L	= Reynolds number based on L
u', v', w'	= rms fluctuating velocity components
U, V, W	= mean velocity components
$\tilde{u}, \tilde{v}, \tilde{w}$	= crossflow plane velocity components
U_∞	= freestream velocity
$\tilde{u}_\theta$	= circumferential crossflow velocity component
x, y, z	= wind-tunnel coordinate system
$\tilde{x}, \tilde{y}, \tilde{z}$	= crossflow plane coordinate system
α	= angle of attack
θ	= circumferential angle measured from windward ray
ξ, η, ζ	= computational curvilinear coordinates
τ_w	= wall skin friction
ρ	= density
ω_x	= axial component of vorticity

I. Introduction

THE motion of a viscous fluid passing by a slender body of revolution is an interesting flow to study from both a fundamental and an applied viewpoint. The complexity of the vortical flow that can arise belies the simplicity of the body shape. In addition, the fluid dynamic elements of this flow are common to those found on the components of many flight vehicles.

The nature of the vortex wake structure that develops on a slender body of revolution (of practical interest) is primarily dependent on the angle of attack, tip geometry, and fineness ratio of the body. Variation in Reynolds numbers can also significantly affect the vortex wake structure through boundary-layer transition effects. The effect of Mach number has been studied by several authors and is understood from a force and moment point of view, but the actual effect of compressibility on the topology of the wake structure needs to be determined.

On an ogive-cylinder of overall fineness ratio (L/D) 4.5 (configuration used in the present study), the events that take place as the angle of attack is increased from 0–90 deg can be associated with a sequence of angle of attack regimes (suggested by Allen and Perkins[1]). At zero angle of attack, the flow is axisymmetric. A small increment in angle of attack produces a crossflow that eventually causes a steady, symmetric longitudinal vortex pair to form on the leeside of the body. The strength of these vortices, called primary vortices, continues to increase with increasing angle of attack. Evidence of the formation of secondary vortices of opposite sense to the primary vortices may be found near the surface of the ogive. At an angle of attack of approximately twice the nose half-angle (35 deg), a disturbance in the neighborhood of the body causes the orientation of the leeside vortices to become asymmetric, but the flow remains steady. For angles of attack greater than about 60 deg, the flow becomes unsteady. As the angle of attack approaches 90 deg, time-dependent vortex shedding occurs in a manner similar to that found for a two-dimensional circular cylinder.

Side forces approaching the magnitude of the normal force have been attributed to the highly asymmetric vortex orientations on the leeside of the body.[2] On bodies of greater fineness ratio, an array of up to seven vortices alternating in sign have been observed.[3] The mechanisms that cause the flow to become asymmetric are not currently understood. Mechanisms have been postulated based on the impulsive flow analogy, which relates the three-dimensional steady flow past a pointed slender body to the two-dimensional unsteady flow around an impulsively started circular cylinder. The relevance of the analogy has not yet been fully demonstrated.

There are a few studies in the literature that directly relate (containing measurements of the velocity field) to the present study. Owen and Johnson[4] used a laser-Doppler velocimeter (LDV) to measure three components of mean and fluctuating velocity in planes at several x/L positions on a body where $L/D = 12$. Additionally, surface hot-film gages were used to measure the surface skin friction. The most significant result of that study was the discovery of a dominant energy peak in the surface skin-friction spectrum associated with the vortex

Presented as Paper 87-2277 at the AIAA 5th Applied Aerodynamics Conference, Monterey, CA, Aug. 17-19, 1987; received Oct. 1, 1987; revision received March 16, 1988.

*Research Scientist.

structure. Wardlaw and Yanta[5] experimentally examined the flow over a slender body at high incidence using a two-component LDV system. Streamlines in a crossflow plane determined from the measured velocity components indicates a vortical flow structure (in the planes) that differs from previously conceptualized flow topologies (see Peake and Tobak[6]). The results presented showed that under certain conditions, the crossflow streamlines at foci in the crossflow planes could sprial outward rather than inward. This event could be explained by showing the concurrent existence of a decelerating streamwise velocity component. This result is unusual and prompted Wardlaw and Yanta to question whether crossflow streamlines are truly representative of three-dimensional streamlines.

The primary objectives of the present work are 1) to perform Navier-Stokes computations of the vortical flow around an ogive-cylinder model at angle of attack and flow conditions matching those of a companion water-tank experiment; 2) to gain confidence in the ability of the code to capture the main features of the flow by comparing the computed and visualized crossflow velocity fields; 3) to gain insight into the structure, origin, and behavior of the vortex flow from detailed examination of the computed flows; and 4) to investigate the effects of Reynolds number variation on the vortex flows in this case of fully laminar boundary-layer separation.

II. Computational-Experimental Approach

Numerical Approach

The flow around a slender body of revolution at moderate to high angles of attack and low Mach number is a complicated vortical flow with viscous effects playing a primary role in the development of the vortical structure. An accurate numerical description of the flow requires the solution of the incompressible Navier-Stokes equations. Flow visualization performed in preparation for this study revealed that the flow about the ogive was steady for angles of attack less than 60 deg; thus, a time-accurate computation is not necessary. For sufficiently low Reynolds number, the flow around the ogive is laminar and turbulence modeling is not required.

In this investigation, the INS3D computer code developed by Kwak, Chang, Shanks, and Chakravarthy is applied to solve the Navier-Stokes equations for flow around an ogive-cylinder body using the method of pseudocompressibility. The numerical approach used in the INS3D computer code is described in great detail in Ref. 7, and the computational aspects specific to the present study are described in Ref. 8. Briefly, the governing equations including the pseudocompressibility terms are written in finite-difference form using central differences for the spatial terms. These equations are approximately factored using the factorization technique of Beam and Warming.[9] Implicit second-order and explicit fourth-order numerical dissipation is added to damp out high-frequency oscillations. The solution is advanced in time until a steady state is reached.

The configuration of the ogive-cylinder model is similar to, and in certain cases identical to, configurations used in past experimental studies.[10] The body is a tangent ogive-cylinder of fineness ratio 3.5 with a cylindrical afterbody of fineness ratio 1.

To accurately capture the variety of flow-length scales, careful attention must be paid to the computational mesh. Near the tip of the ogive, a region of high gradients exists owing to the presence of a stagnation point and, in addition, because the tip is the origin of the leeside vortices. Experiments[11] have demonstrated that very small changes in the tip geometry can have a dramatic effect on the orientation of the leeside vortices. In this study, grid points were clustered at the tip and rear of the afterbody using a cosine point distribution. Figure 1 shows the mesh used for this study. The grid is composed of 49 by 39 by 68 points in the normal, axial, and tangential directions, respectively.

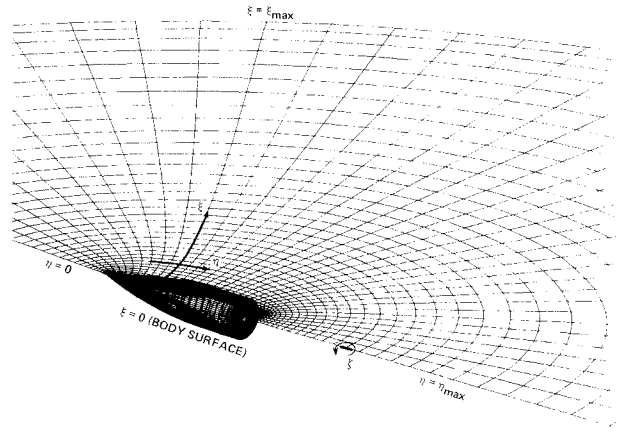

Fig. 1 Perspective view of the wrapped computational mesh.

Near the surface of the ogive, the mesh spacing was chosen to resolve the viscous effects present in the boundary layers. After extensive study of the effects of grid spacing on accuracy, it was decided that at least seven grid points needed to be placed in the attached boundary layer normal to the surface to capture the large gradients present.

The numerical boundary conditions consist of specifying conditions on the pressure and velocities on the body surface, at the inflow and outflow boundaries, and near the grid axis of revolution. In addition to these four boundary conditions, a circumferential periodicity condition was imposed. These conditions, which do not enforce symmetry of the solution, are explained in greater detail in Ref. 8. At the beginning of the convergence process, the dependent variables are initialized to 1.0 in the interior of the computational domain.

There are several possible sources of error in the numerical method that may affect the solution accuracy. These errors include the effects of the second- and fourth-order artificial viscosity, truncation error, grid resolution, symmetry bias errors, and boundary-condition numerical errors. The effects of the artificial viscosity and truncation errors are discussed in Refs. 12 and 13. These effects were shown by analysis and example to be minimal, provided that the level of explicit artificial viscosity acting on the pressure is allowed to decay during the solution process. To test the resolving capability of the mesh, the number of grid points was cut in half, and the impact on the solution was observed. The effect was found to be minor. The bias errors are thought to be minimal owing to the high degree of symmetry in the solution. Estimates of the effects of boundary condition errors are difficult to quantify and are a continuing area of research.

Towing-Tank Study

A companion experimental study was performed in a 55-gallon water-towing-tank apparatus (Fig. 2) using a 4-in. long aluminum ogive-cylinder model. The Reynolds number and model configuration were identical to those in the computation, aside from a small sting that was used to support the model. Flow in the crossflow plane was visualized by taking a time exposure of the induced motion of a saltwater suspension of neutrally buoyant Pliolite particles (approximate diameter of 0.0035 in.) illuminated by laser light. To improve the laser sheet crossflow plane visualization, a cylindrical lens in combination with a short focal-length lens was used to produce a 0.3-in.-thick laser light sheet. The model was moved through the water by a traversing mechanism, and short time-exposure photographs of the induced particle motion were taken.

The particle streaks recorded on the photographs correspond to projections of the instantaneous three-dimensional velocity on a plane orthogonal to the body axis. The camera and laser sheet were moved with the model to produce the instantaneous streamline pattern as would be seen by an observer in the model's frame of reference. After transient ef-

fects introduced at the startup of the motion had diminished and the flow had reached steady state, the particle streaks indicated a steady streamline pattern. Information concerning the velocity direction and magnitude could be obtained from the image by measuring the length and orientation of the particle streaks.

Wind-Tunnel Studies

Two sets of wind-tunnel experiments were conducted during this investigation. In the first set, mean velocity and pressure were measured in crossflow planes using a seven-hole pressure probe. The second set of experiments involved using a hot-wire anemometer to measure velocity as a function of time at selected points in the vortex core.

Measurements were carried out in a 15-in. by 15-in., low-turbulence wind tunnel (Fig. 3). Maximum freestream turbulence level of this facility as measured by a hot-wire anemometer is 0.15%. Reference 14 describes the seven-hole probe calibration technique that was developed specifically for this set of measurements. As shown in this reference, the flow angle (flow sideslip angle and angle of attack relative to the probe) could be measured to within 0.4 deg. The seven-hole probe diameter is 0.12 in.

A three-axis traversing system was used to move the probe to positions in the crossflow plane at several $\tilde{x}/L$ stations. This system was completely enclosed in a pressure-tight box that rested on top of the test section. Probe access to the test section was via movable slots in the top wall of the test section. Positioning accuracy of the the optically encoded traversing system was determined to be within 0.0005 in.

The model configuration was similar to the computational and towing-tank configurations aside from the sting support system. Overall length of the model was 9 in., and the diameter of the cylindrical afterbody portion of the model was 2 in. Figure 4 shows the model, measurement plane locations, and the two relevant coordinate systems. The test involved surveys of the crossflow plane at two stations on the body and one in the wake for angles of attack of 30 and 45 deg at $Re_L = 820{,}000$ ($Re_D = 164{,}000$). No trips were used to stabilize the vortex positions or cause boundary-layer transition. Smoke-flow visualization tests showed that the vortices remained in a fixed orientation at the two angles of attack of interest; hence, it was decided that trip strips should not be used. Model blockage, based on the projected frontal area of the model, was 2.4 and 3.5% of the cross-sectional area of the test section for angles of attack of 30 and 45 deg, respectively.

To verify the assumption that the vortical flow was steady under these test conditions, a constant temperature hot-wire anemometer was used to measure the velocity fluctuations at several points in the flowfield. Results of these measurements are discussed in the following section.

III. Numerical and Experimental Results

Computational and Towing-Tank Results

Analysis of three-dimensional results is a complicated task due to the inherent difficulties associated with presenting and understanding physical quantities that vary in three spatial directions. Two different approaches to presenting the data are used in this section to cope with the difficulties. In the first approach, data are presented in two-dimensional crossflow planes at different locations along the body. Although this approach has limitations, it is very useful for a flow that is conical or where the flow in the third dimension is slowly evolving. The second approach involves the three-dimensional display of data such as particle path lines. Three-dimensional displays of data can sometimes be deceptive due to perspective difficulties, but they overcome the limitation of the first approach.

The two cases computed were for an $L/D = 3.5$ ogive with a cylindrical afterbody of $L/D = 1.0$ at angle of attack of 30 and 45 deg at $Re_L = 1000$ ($Re_D = 220$). Selected comparisons of the computed crossflow velocity vectors with the corresponding

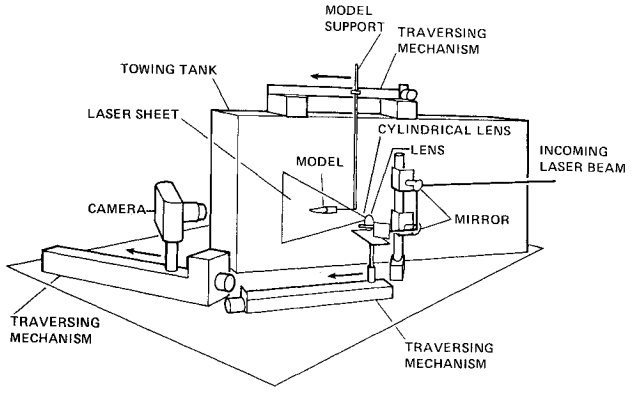

Fig. 2 Perspective view of the towing tank with model.

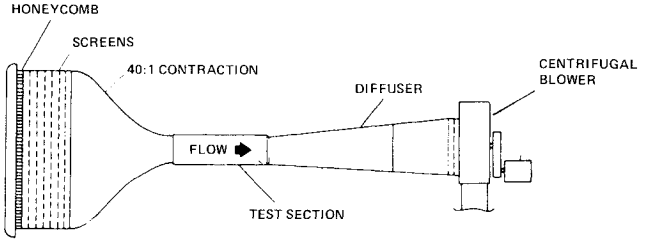

Fig. 3 Plan view of the 15 in. × 15 in. wind tunnel.

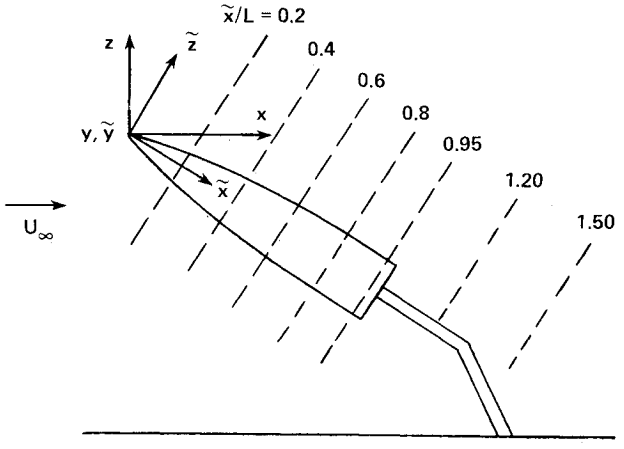

Fig. 4 Ogive-cylinder model and coordinate systems.

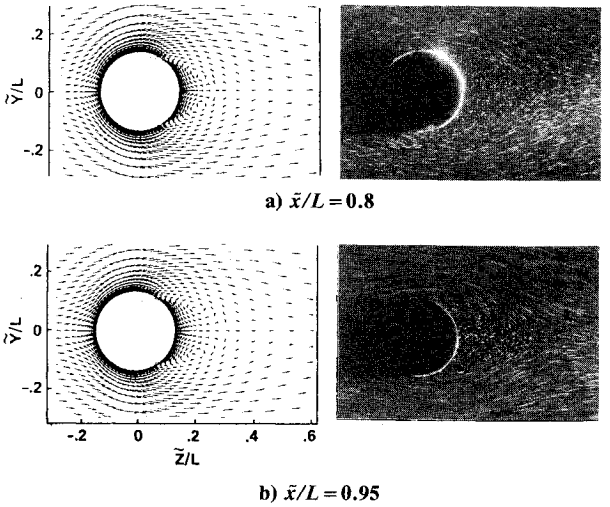

a) $\tilde{x}/L = 0.8$

b) $\tilde{x}/L = 0.95$

Fig. 5 Comparison of computed and visualized crossflow velocity vectors at $\alpha = 30$ deg, $Re_L = 1000$.

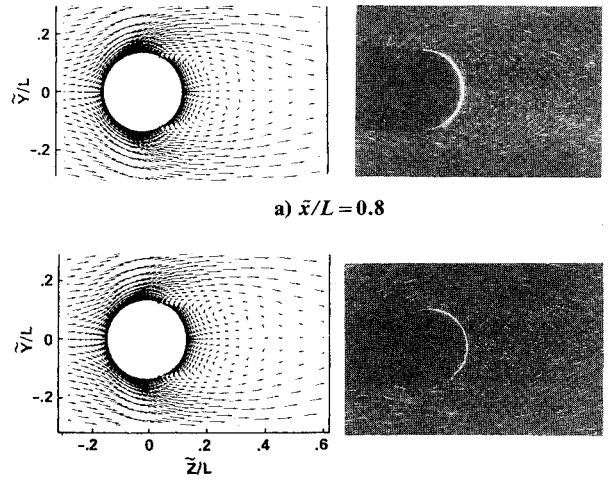

a) $\tilde{x}/L = 0.8$

b) $\tilde{x}/L = 0.95$

Fig. 6 Comparison of computed and visualized crossflow velocity vectors at $\alpha = 30$ deg, $Re_L = 1000$.

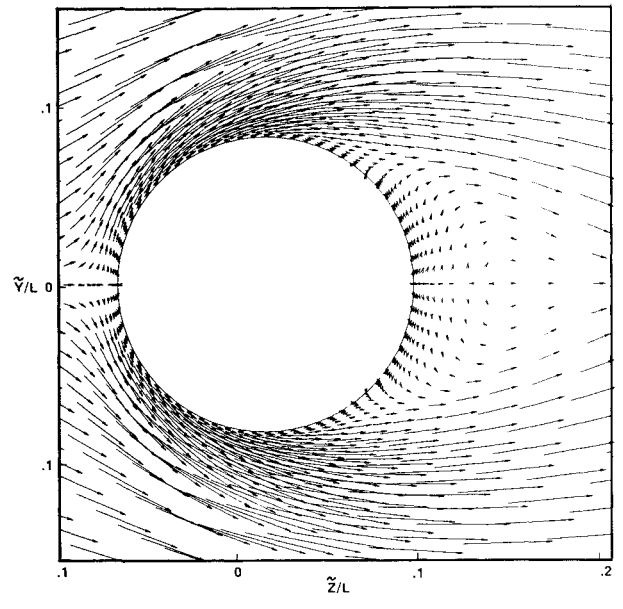

Fig. 7 Closeup of the velocity field near the surface in the crossflow plane at $\tilde{x}/L = 0.4$, $\alpha = 45$ deg, $Re_L = 1000$.

projected three-dimensional velocity obtained from the towing-tank study are presented in Fig. 5 for $\alpha = 30$ deg and in Fig. 6 for α-45 deg ($\tilde{y}$ and $\tilde{z}$ denote crossflow-plane coordinates; see Fig. 4). These figures show the development of the flow in crossflow planes at different axial stations along the body. In general, the flow development is similar for the two angles of attack. In both cases, the vortices assume a symmetric orientation. Near the tip at $\tilde{x}/L = 0.2$ (not shown) no recirculating flow region is present. At this station the flow resembles the initial flow observed on an impulsively started, two-dimensional circular cylinder. The second station at $\tilde{x}/L = 0.4$ shows the beginning signs of a recirculation zone, and for the $\alpha = 45$ deg case evidence of a saddle point is present on the leeward axis of symmetry. A closeup view of this flow is shown in Fig. 7. In addition to the saddle point on the leeward side, the flow on the windward side of the body shows a zero circumferential velocity point, development of the crossflow boundary layer on either side of this point, and acceleration of the crossflow as it passes around the body. At $\tilde{x}/L = 0.8$ (Figs. 5a and 6a), the two flows show distinctive separation points, saddle points, and vortex core centers for both cases. The final frames ($\tilde{x}/L = 0.95$) (Figs. 5b and 6b) vividly

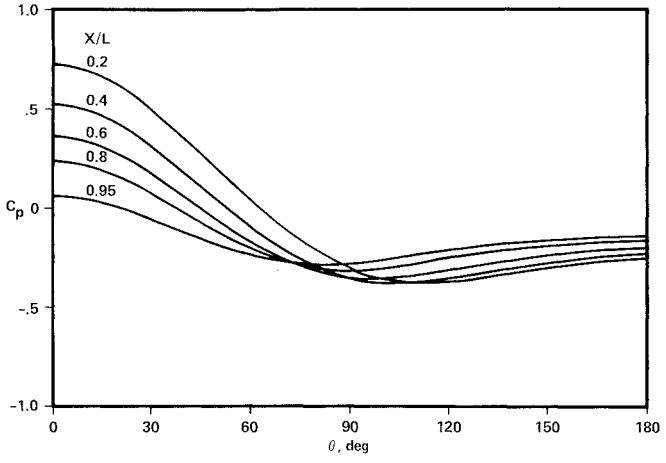

a) $\alpha = 30$ deg

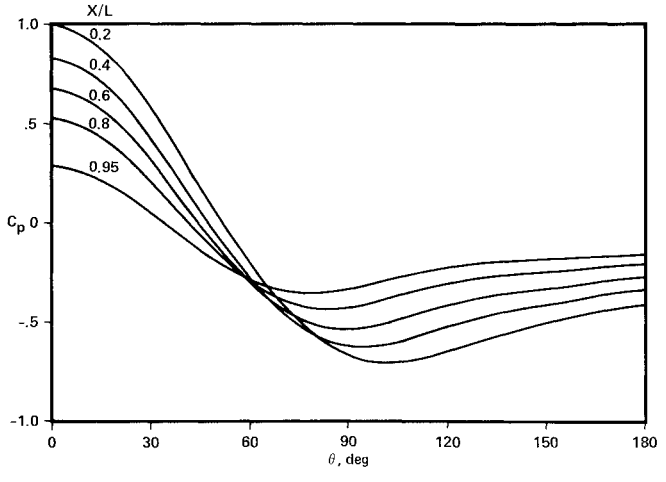

b) $\alpha = 45$ deg

Fig. 8 Circumferential surface pressure in the crossflow plane at various stations along the body at $Re_L = 1000$.

show the primary vortices near their fully developed state. In addition, the crossflow separation points on the surface have moved in the windward direction, creating pockets of nearly stagnant fluid near these points, but no evidence of secondary vortices is present in either the experimental or the computational results.

In general terms, the sequence of events that occurs during the development of the vortex flowfields is the same for the two cases studied. The primary difference between the cases is the rate at which the vortices develop along the length of the ogive (i.e., slower development for the lower angle of attack case). This result is consistent with that suggested by the impulsive flow analogy.

Computed surface pressure plots are shown in Fig. 8 for the two cases investigated. Considering the $\alpha = 45$ deg case (Fig. 8b), one can deduce several interesting features about the vortical flow from the crossflow pressure distribution. As expected, at each value of $\tilde{x}/L$ the maximum pressure point is located on the windward ray ($\theta = 0$ deg). The maxima decrease in magnitude progressively from the tip to the end of the body along the windward ray. Near the tip of the ogive ($\tilde{x}/L = 0.2$), the circumferential pressure variation is the largest of the five stations considered, and the circumferential pressure gradient remains favorable until approximately $\theta = 115$ deg. At $\tilde{x}/L = 0.95$, the circumferential pressure variation is the smallest and the onset of adverse pressure gradient occurs at approximately $\theta = 80$ deg. The behavior of the pressure at the intermediate stations falls between these two extremes. These same trends apply to the $\alpha = 30$ deg case (Fig. 8a) and are the expected trends based on the impulsive flow analogy.

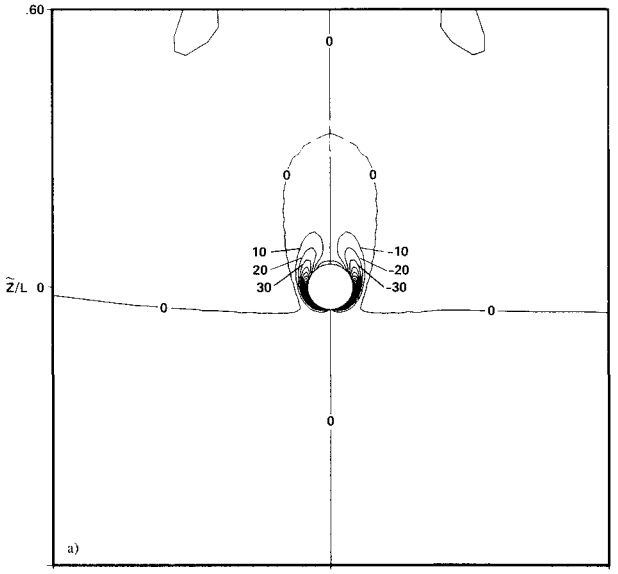

a) $\tilde{x}/L = 0.2$

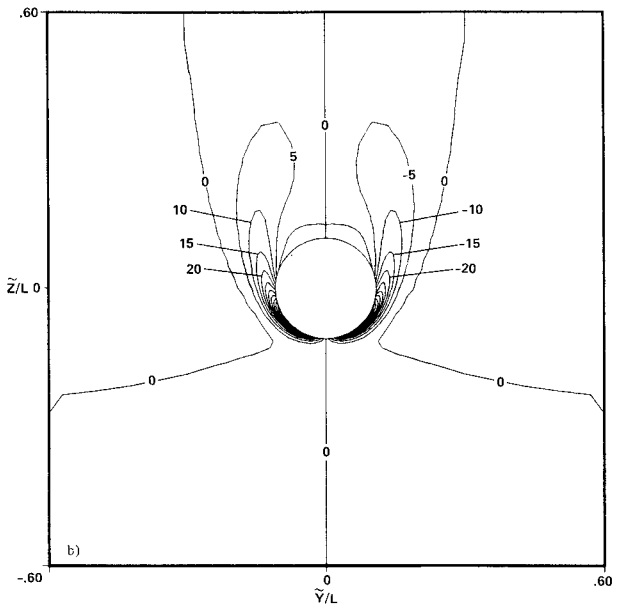

b) $\tilde{x}/L = 0.95$

Fig. 9 Axial vorticity contours in the crossflow plane at $\alpha = 45$ deg, $Re_L = 1000$.

Vorticity contours of the flowfield provide further insight into the way in which the flow develops. Computed axial vorticity contours (ω_x) for the $\alpha = 45$ deg case (at $\tilde{x}/L = 0.2$ and 0.95) are presented in Fig. 9. The intermediate stations have the same basic character of these two planes. At the windward ray, the vorticity is a minimum, then progressively increases to a maximum, and then decreases back to zero at the leeward ray. The vorticity maxima are located at approximately 45 deg on either side of the windward ray. These vorticity plots are very reminiscent of typical two-dimensional cylinder vorticity contours. The vorticity is diffuse and not concentrated in the core region, contrary to what might be expected.

Three dimensional views of the flowfield are presented in Fig. 10. Particles were released from points in the windward boundary layer at several axial positions. The particles then passed around the body, were entrained into the leeside vortical flow, and then continued downstream. The differences between the two cases are most evident in these particle pathlines. The vortical flow appears to be stronger for the $\alpha = 45$ deg case, (Fig. 10b) and the vortical flow also develops over a shorter distance.

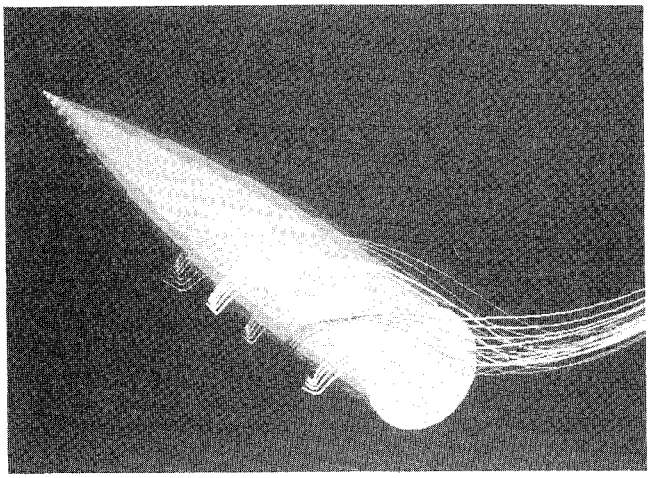

Fig. 10a Computed particle path lines for $\alpha = 30$ deg.

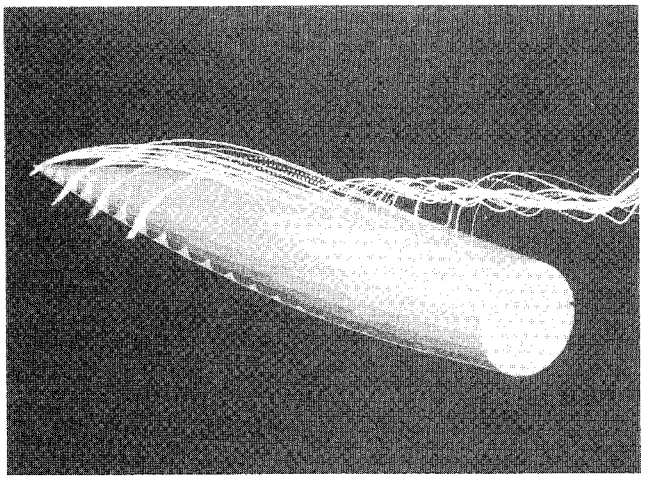

Fig. 10b Computed particle path lines for $\alpha = 45$ deg.

Crossflow Streamlines

In several recent studies of vortex flows similar to the present one, under certain conditions, streamlines in crossflow planes were found to spiral outward from the foci in the planes. As demonstrated by Wardlaw and Yanta,[5] the spiral direction could be verified by applying the continuity equation. If $d\tilde{u}/d\tilde{x}$, which is a measure of the rate of change of $\tilde{u}$ with $\tilde{x}$, is greater than zero throughout the region occupied by the vortex, then the crossflow steamlines must spiral inward. In the present study, the sign of $d\tilde{u}/d\tilde{x}$ was checked by plotting contours (not included) of $d\tilde{u}/d\tilde{x}$ in the crossflow plane. Values of $d\tilde{u}/d\tilde{x}$ were found to be small in magnitude but greater than zero in regions near the core of the vortex for the computational results. Computing $d\tilde{u}/d\tilde{x}$ for the wind-tunnel results (presented in the following sections) was a difficult task owing to data accuracy considerations, however; at several points in the core region $d\tilde{u}/d\tilde{x}$ was definitely positive. Hence, under all of the test conditions of the present study, it is believed that streamlines in the crossflow planes spiral inward.

Surface Flow Patterns

Since surface oil patterns or the computational analog of surface particle pathlines often are used in an attempt to understand and classify different types of two- and three-dimensional flows, it is important to understand what the pathlines indicate about the flowfield. It is generally assumed that by observing the surface particle pathlines conclusions can be drawn about the direction of the skin-friction vector. This assumption is valid but, as will be shown, with the exception of locating singular points (saddles, nodes, etc.) in the surface shear-stress field, little can be concluded about varia-

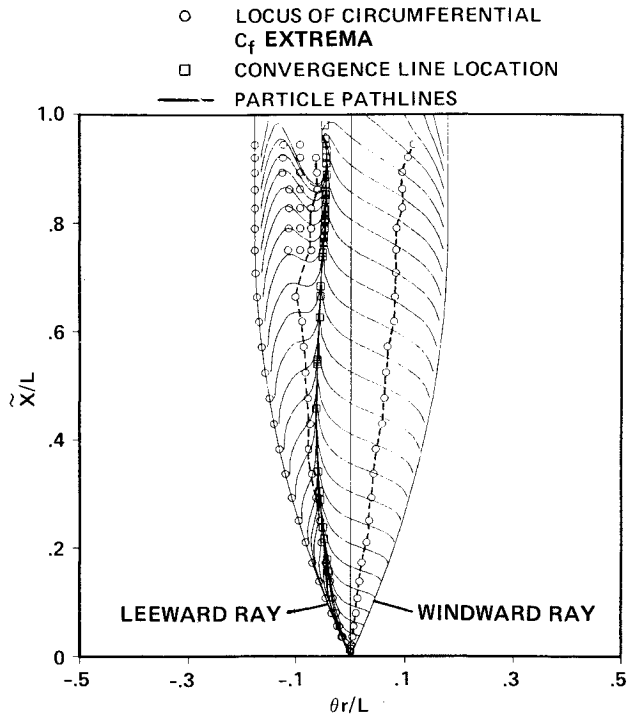

Fig. 11 Unwrapped half-surface showing computed surface-particle path lines for $\alpha = 45$ deg, $Re_L = 1000$.

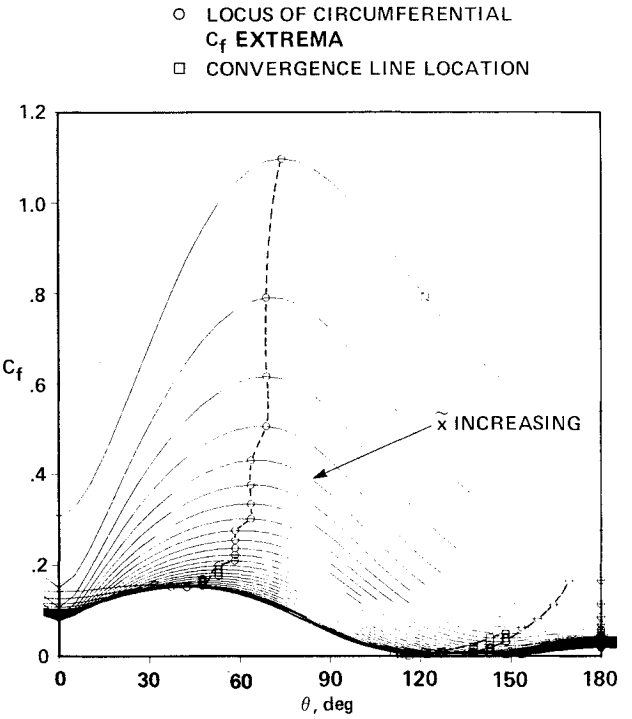

Fig. 12 Skin-friction absolute magnitude for $\alpha = 45$ deg, $Re_L = 1000$.

tions in the skin-friction absolute magnitude by observing the surface flow pattern. The exception to this rule is the special case of two-dimensional separation.

In a flow that separates two dimensionally, associated with the flow departure from the surface is a break (or point) in the surface particle pathlines. These points form a locus where the magnitude of the skin friction is zero. Along this locus (by definition), the skin friction is also a streamwise minimum.

In a three-dimensional, globally separated flow (see Ref. 6. for definition of terms), a saddle point must be present in the surface particle pathlines. Existence of saddle points implies that there is streamwise flow reversal. Only at the singular points, such as at a saddle, is the skin friction equal to zero and also equal to a local minimum.

Under the conditions of the present investigation (local separation), no flow reversal in the streamwise direction exists on the leeside of the body. Thus, nowhere (except at the ends of the body) is the magnitude of the skin friction equal to zero. Consequently, there are no singular points in the surface particle pathlines. In addition, a local skin-friction minimum is not directly associated with the departure of fluid from the surface of the model along the convergence line (also known as a bifurcation line).

Presented in Fig. 11 are the computed surface particle pathlines that were produced by releasing particles on the surface and then by following their trajectories. These results are similar to the oil-flow results presented in recent studies of pointed bodies of revolution.[10] The circular symbols on this figure show locations of the circumferential skin-friction extrema. The particle trajectories converge toward each other on the surface and ultimately form a common line. As can be seen in this figure, the position of the locus of skin-friction minima does not coincide with the convergence line.

Presented in Fig. 12 is the absolute skin-friction magnitude as a function of θ at different $\tilde{x}/L$ positions. The magnitude of skin friction has been defined as

$$C_f = \frac{\tau_w}{1/2\rho U^2_\infty} = \frac{\mu[(d\tilde{u}_\theta/dr)^2 + (d\tilde{u}/dr)^2]^{1/2}}{1/2\rho U^2_\infty}$$

Also shown is the line where the surface pathlines converge. It is extremely difficult to quantify the mathematical characteristics of this convergence line. Correlations of the characteristics of this line with minimas or skin-friction zeros have not been found. As evident in Fig. 12, the skin friction is nonzero everywhere on the surface except in the base region. The locus of skin-friction minimums lies slightly toward the leeward ray and nearly parallels the line of convergence.

As shown in Ref. 15, explicit artificial viscosity (a dissipative term) can have a substantial impact on surface skin-friction patterns. It also was demonstrated in this reference that this difficulty may be overcome by reducing the magnitude of artificial viscosity near the surface. This modification was incorporated in the numerical procedure and proved to have little effect on the solution.

An explanation for why the line of convergence is not a line of minimum skin friction can be understood by considering that along the line of convergence, the $d\tilde{u}/dr$ skin-friction contribution continuously decreases from tip to the base of the body and the $d\tilde{u}_\theta/dr$ contribution does not have a circumferential minimum near the line of convergence location (except near the base of the body). Therefore, the vector magnitude of the skin friction cannot form a locus of skin-friction minimas.

In the limit of an infinitely long body, there is reason to believe that the line of convergence and locus of skin-friction minimas should coincide at infinity. Figures 11 and 12 support this hypothesis. Although the skin-friction gradients are very small, it appears that the locus of skin-friction is asymptotically approaching the line of convergence (on the cylindrical portion of the body).

This discussion points out some of the fundamental differences between local and global separation. Strictly speaking, the term separation only should be used to describe flows with streamwise flow reversal. Acceptance of this distinction would serve to distinguish flows that have a direct correlation between properties of the surface particle trajectories and streamline behavior of those that do not.

Wind-Tunnel Results

Presented in Fig. 13 are the crossflow velocity vectors for $\alpha = 30$ deg case at $Re_L = 820{,}000$. Referring to the low Reynolds number results shown in Fig. 5 (at the same angle of attack and X/L position), it is interesting to see that sizes of

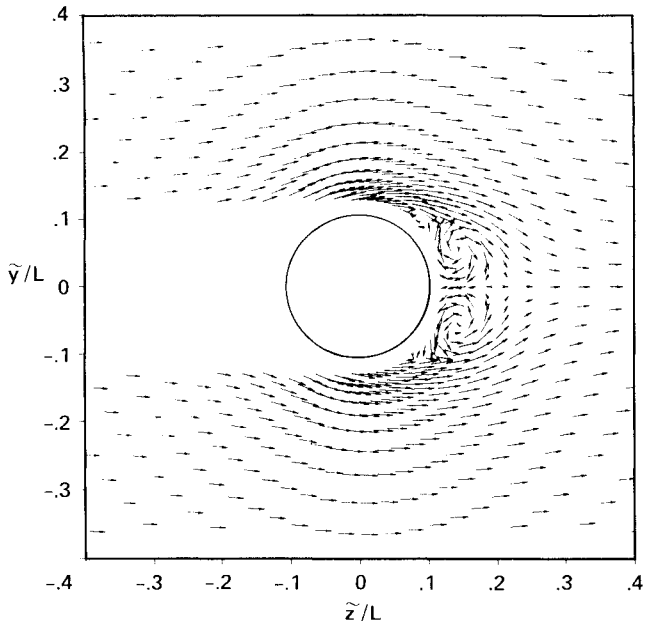

a) $\tilde{x}/L = 0.8$

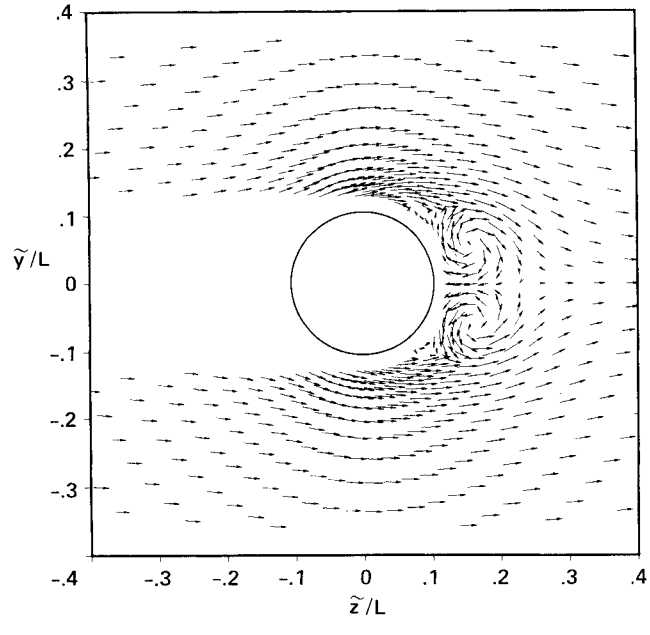

b) $\tilde{x}/L = 0.95$

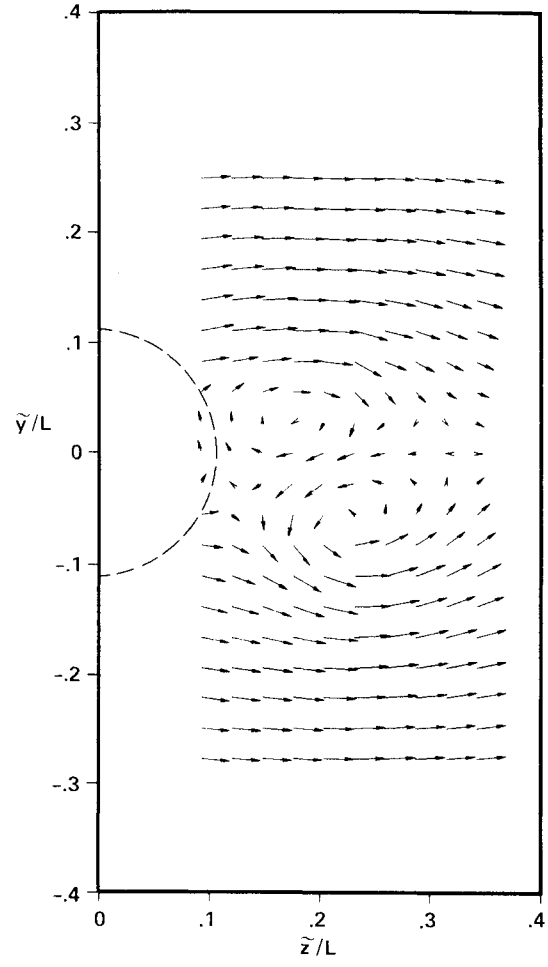

c) $\tilde{x}/L = 1.5$

Fig. 13 Measured crossflow velocity vectors at $\alpha = 30$ deg, $Re_L = 820{,}000$.

the primary vortices are similar. Based on the impulsive flow analogy, one might have expected the location of the saddle point to be further away from the surface of the body for the higher Reynolds number. Tobak has suggested that the distance to the saddle point may asymptotically approach a constant value as the Reynolds number is increased. This hypothesis is suggested by an experimental study of two-dimensional circular cylinders wake lengths. In Ref. 16, data are presented that show that the time-averaged saddle point location approaches an asymptote with increasing Reynolds number. A study specifically designed to determine the saddle point locations on bodies of revolution with variation in Reynolds number is needed to validate this suggestion.

A plane of data was also taken in the wake of $\tilde{x}/L = 1.5$. These data show that the vortices have assumed an asymmetric orientation in the wake. It is interesting to note that this effect does not seem to have propagated upstream in an observable fashion (compare Figs. 13b and 13c). A possible explanation of this result is that although the vortices appear to be symmetric on the body, there must be a small degree of asymmetry. In the wake, the slight circulation differential between the two counter-rotating vortices causes one to move around the other. In an inviscid sense, these vortices must be held in equilibrium by image vortices or else they would not be steady. The sting support should not influence this result to a high degree. The support system is symmetrically located with respect to the model symmetry plane and relatively far from the plane of data.

At $\alpha = 45$ deg, the leeside vortex flow has changed completely as shown in Fig. 14. The vortex orientation is asymmetric both above the body and in the wake. Also, it is difficult to distinguish vortex core regions. Comparison of Figs. 14 with 6 demonstrates that there is a Reynolds number effect. At $Re_L = 1000$, the computation and the towing-tank experiment show a symmetric leeside vortex orientation, whereas at $Re_L = 820{,}000$, the flow is highly asymmetric. The importance of this result is that in order to understand, model, or compute asymmetric flows, and also probably the passage from the symmetric to the asymmetric state, viscous effects must be incorporated in the analysis.

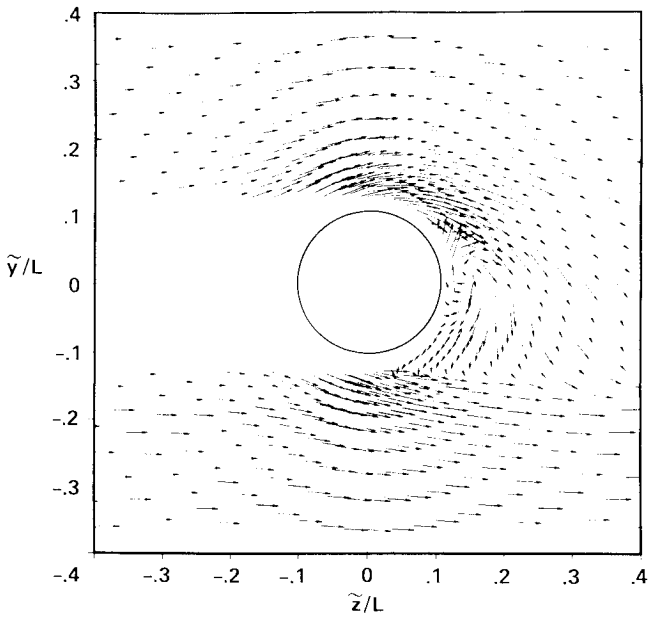

a) $\tilde{x}/L = 0.8$

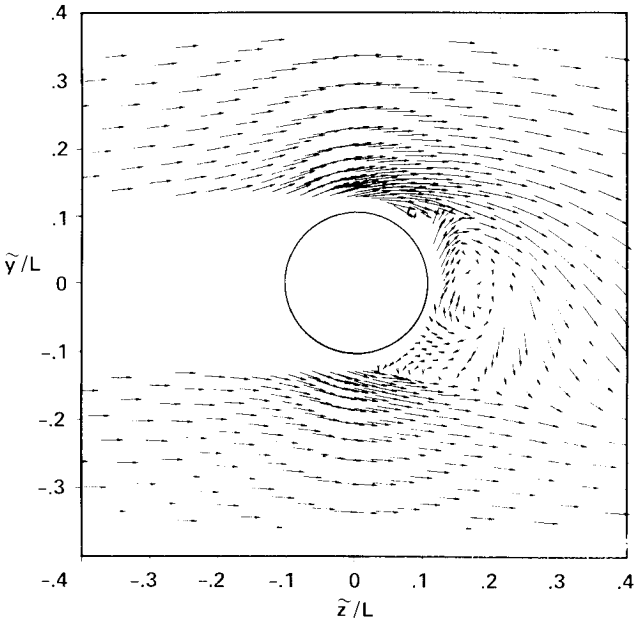

b) $\tilde{x}/L = 0.95$

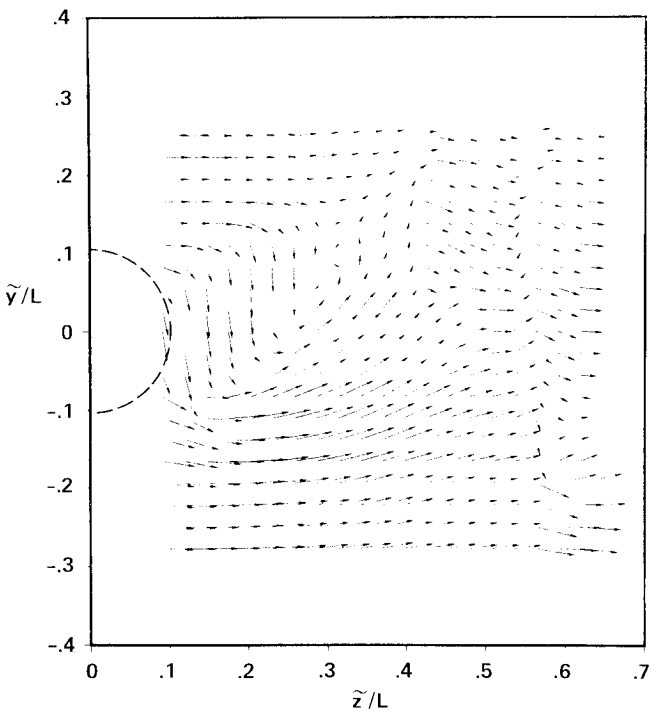

c) $\tilde{x}/L = 1.2$

Fig. 14 Measured crossflow velocity vectors at $\alpha = 45$ deg, $Re_L = 820{,}000$.

Vortex Core Velocity Fluctuations

Since the crossflow Reynolds number of the wind-tunnel experiment is less than the transition Reynolds number for two-dimensional circular cylinders, ($Re_{D,\ \mathrm{crit}} = 450{,}000$), the boundary layers of the windward side should be laminar when they separate. This assertion is supported by the measured separation point location of $\theta = 120$ deg for the $\alpha = 30$ deg cases (computation and wind-tunnel experiment) at $\tilde{x}/L = 0.95$. Generally, laminar boundary layers cannot remain attached in strong adverse pressure gradients; hence, if the flow had become transitional before it separated, the separation location should be closer to $\theta = 140$ deg (see Ref. 17).

Presented in Fig. 15 are the power spectra measured by a hot-wire anemometer in one of the vortex cores at the $\tilde{x}/L = 0.95$ station. The spectras show a sharp dropoff from the mean velocity followed by a continuous rolloff of the signal with frequency. The shape of these spectra indicate that the core flow is turbulent but steady in the mean (i.e., no low-frequency wandering). A possible explanation for this level of turbulence is that the strong mean shear in the leeside vortices produces turbulence. The u'/U quantities measured in the cores at $\tilde{x}/L = 0.95$ are 0.104 at $\alpha = 30$ deg and 0.135 at $\alpha = 45$ deg angle of attack (approximately 100 times greater than the freestream wind-tunnel turbulence level). A dominant energy

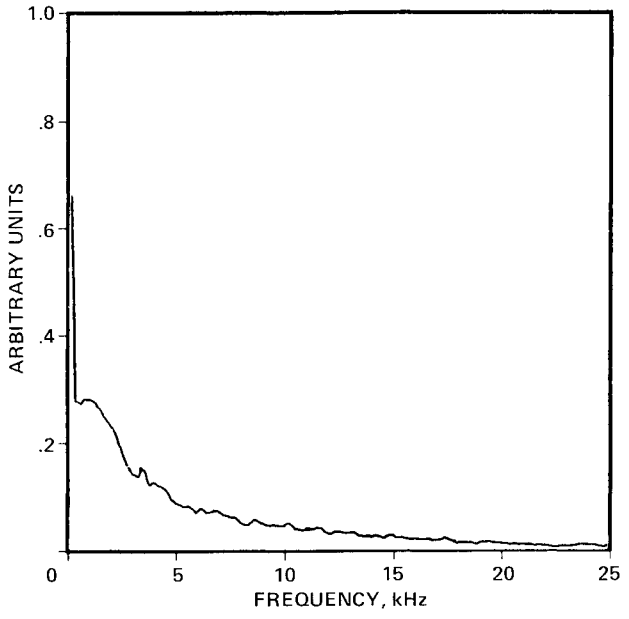

a) $\alpha = 30$ deg

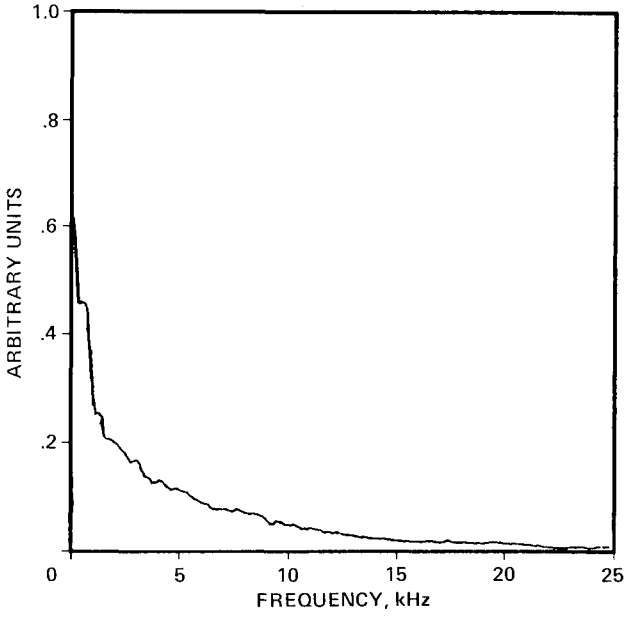

b) $\alpha = 45$ deg

Fig. 15 Measured U velocity spectra in vortex core at $\bar{x}/L = 0.95$, $Re_L = 820{,}000$.

peak cannot be deciphered from these spectra. This result is interesting, considering that in Ref. 2 a Stouhal number of 0.2 (based on the crossflow velocity) was determined from fluctuating skin-friction measurements on a tangent ogive-cyliner. It is possible that Owen and Johnson detected an unsteady vortex shedding that is not present in the current study. A thorough experimental program involving velocity correlation measurement should be undertaken to answer these questions definitively. Recent measurements[18] of velocity fluctuations in the wakes of inclined bodies of revolution indicate that the L/D ratio of the body can have a significant impact on degree of wake unsteadiness.

IV. Conclusions

The flow over a pointed body of revolution has been studied from an experimental and computational viewpoint. Comparisons of computational results based on the Navier-Stokes equations and flow visualization results are favorable and tend to validate the accuracy of the computation in a qualitative manner. Comparisons of the low Reynolds number computational and towing-tank results with the moderate Reynolds number wind-tunnel results show a Reynolds number effect that demonstrates the importance of including the viscous effect in analyses of the onset of vortex asymmetry. A study of the surface skin friction indicates that no general correlation exists between skin-friction magnitude and the location of the line of convergence. Analyses of the spiral directions of crossflow streamlines show an inward spiral under all test conditions studied. Velocity spectrum measurements in the core of the leeside vortices show that a crossflow Reynolds number less than the critical Reynolds number for boundary-layer transition, the core of the leeside vortice contain turbulence.

References

[1]Allen, H. J. and Perkins, E. W., "Characteristics of Flow Over Inclined Bodies of Revolution," NASA RM-A50L07, March 1951.

[2]Ericsson, L. E. and Reding, J. P., "Vortex-Induced Asymmetric Loads in 2-D and 3-D Flows," AIAA Paper 80-0181, Jan. 1980.

[3]Thomson, K. D. and Morrison, D. F., "The Spacing and Position and Strength of Vortices in the Wake of Slender Bodies at Large Incidence," *Journal of Fluid Mechanics*, Vol. 50, Pt. 4, Aug. 1971, pp. 751–783.

[4]Owen, K. F. and Johnson, D. A., "Wake Vortex Measurements of Bodies at High Angle of Attack," AIAA Paper 78-23, Jan. 1978.

[5]Wardlaw, A. B. and Yanta, W. J., "Asymmetric Flowfield Development on a Slender Body at High Incidence," *AIAA Journal*, Vol. 22, Feb. 1984, pp. 242–249.

[6]Peake, D. J. and Tobak, M., "Three-Dimensional Interactions and Vortical Flows with Emphasis on High Speeds," AGARDograph No. AG-252, July 1980.

[7]Kwak, D., Chang, J. L. C., Shanks, S. P., and Chakravarthy, S. R., "A Three-Dimensional Incompressible Navier-Stokes Flow Solver Using Primitive Variables," AIAA Paper 84-0253, Jan. 1984.

[8]Zilliac, G. G., "A Computational/Experimental Study of the Flow Around a Body of Revolution at Angle of Attack," NASA TM-88329, Sept. 1986.

[9]Beam, R. M. and Warming, R. F., "An Implicit Finite-Difference Algorithm for Hyperbolic Systems in Conservation Law Form," *Journal of Computational Physics*, Vol. 22, Sept. 1976, pp. 87–110.

[10]Keener, E. R., "Flow Separation on Symmetric Forebodies," NASA TM-86016, Jan. 1986.

[11]Lamont, P. J., "Pressures Around on Inclined Ogive Cylinder with Laminar, Transitional, or Turbulent Separation," *AIAA Journal*, Vol. 20, Nov. 1982, pp. 1492–1499.

[12]Kwak, D. and Chang, J. L. C., "A Three-Dimensional Incompressible Flow Solver, Parts 1 and 2," Notes for the Workshops on CFD in Aerospace Design Workshop on CFD in Aerospace Design, Univ. of Tenn. Space Institute, Tullahoma, TN, 1985.

[13]Rogers, S. E., Kwak, D., and Kaul, U., "On the Accuracy of the Pseudo-compressibility Method in Solving the Incompressible Navier-Stokes Equations," AIAA Paper 85-1689, July 1985.

[14]Zilliac, G. G., "Calibration of Seven-Hole Pressure Probes for Use in Fluid Flows with Large Angularity," NASA TM 102200, Aug. 1989.

[15]Kaynak, U., Holst, T. L., and Cantwell, B. J., "Computation of Transonic Separated Wing Flows Using an Euler/Navier-Stokes Zonal Approach," NASA TM 883311, July 1986.

[16]Nishioka, M., and Santo, H., "Mechanism of Determination of the Shedding Frequency of Vortices Behind a Cylinder at Low Reynolds number," *Journal of Fluid Mechanics*, Vol. 89, Pt. 1, 1978, pp. 49–60.

[17]Peake, D. J., Owen, K. F., and Higuchi, H., "Symmetrical and Asymmetrical Separations About a Yawed Cone," NASA TN 78532, Sept. 1978.

[18]Degani, D. and Zilliac, G. G., "experimental Study of Nonsteadiness of the Flow-Around an Ogive-Culinder at incidence," AIAA Paper 88-4330, Aug. 1988.